Research Square

Preprints are preliminary reports that have not undergone peer review.
They should not be considered conclusive, used to inform clinical practice,
or referenced by the media as validated information.

Inferring the internal functional organization of peripheral nerves for selective electrical stimulation

Laura Toni
Scuola Superiore Sant'Anna
Veronica Fossati
Scuola Superiore Sant'Anna
Claudio Verardo
Scuola Superiore Sant'Anna
Elena Losanno
Scuola Superiore Sant'Anna
Silvestro Micera
Scuola Superiore Sant'Anna
Simone Romeni
romeni.simone@hsr.it

Vita-Salute San Raffaele University

Article

Keywords:

Posted Date: September 25th, 2026

DOI: https://doi.org/10.21203/rs.3.rs-10943457/v1

License: This work is licensed under a Creative Commons Attribution 4.0 International License.
Read Full License

Additional Declarations: Competing interest reported. S.M. and S.R. are co-authors of a patent (WO2024095142A2) including the description of the localization method presented in this manuscript.

Inferring the internal functional organization of peripheral nerves for selective electrical stimulation

Laura Toni[1,2]*, Veronica Fossati[1,2]*, Claudio Verardo[2], Elena Losanno[2], Silvestro Micera[1,2,3], Simone Romeni[1]

[1] Modular Implantable Neurotechnologies (MINE) Laboratory, Università Vita Salute San Raffaele & Scuola Superiore Sant'Anna, Milano, Italy

[2] The BioRobotics Institute, Health Science Interdisciplinary Research Center, and Department of Excellence Robotics and AI, Scuola Superiore Sant'Anna, Pisa, Italy

[3] Bertarelli Foundation Chair in Translational Neuroengineering, Neuro-X Institute, Ecole Polytechnique Federale de Lausanne (EPFL), Lausanne, Switzerland

* These authors contributed equally

Corresponding author: Simone Romeni (romeni.simone@hsr.it)

Abstract

Electrical stimulation of peripheral nerves can restore motor function in individuals with upper limb paralysis, but its effectiveness relies on selectively activating specific muscles. Computational models can accelerate the design of stimulation protocols when the nerve's internal functional organization is known. However, this organization cannot currently be determined in patients. To address this limitation, we introduce INFORM (Inference of Neural Functional Organization from Recruitment Matching), a platform that reconstructs nerve functional organization from post-implantation electrode calibration data. We validate the framework in silico using both simplified and anatomically realistic nerve sections, including scenarios with uncertainty in the implanted nerve structure. We then design stimulation protocols based on the inferred models and evaluate their performance against the ideal case of fully known nerve organization. INFORM reliably reconstructs functional organization and enables the optimization of stimulation protocols that perform only marginally worse than those derived from perfect anatomical and functional knowledge. These results support the development of scalable, clinically deployable neuroprosthetic systems by enabling patient-specific optimization of stimulation protocols without requiring direct knowledge of nerve internal anatomy, thereby reducing calibration time, improving selectivity, and facilitating translation across diverse anatomical conditions and clinical settings.

Introduction

Many traumatic and non-traumatic neurological conditions, including stroke, traumatic brain injury, spinal cord injury, and peripheral nerve damage, can lead to motor impairments and, in severe cases, paralysis [1], [2], [3]. Restoring motor function remains a major challenge in neurorehabilitation, particularly for the upper limbs [4], [5]. Electrical stimulation can partially restore movement by injecting artificial motor commands into residual neural pathways. To effectively elicit muscle contractions, stimulation is typically applied distal to the lesion, making peripheral nerve stimulation (PNS) a promising approach, as it requires only an intact distal nerve segment and preserved muscle contractility [6]. PNS has demonstrated neuroprosthetic potential across multiple conditions, including spinal cord injury [7], [8], stroke [9], and peripheral nerve damage [6], [10].

PNS can be delivered via implanted or transcutaneous interfaces, producing different muscle activation patterns depending on the stimulation protocol. Achieving functional movements requires selective stimulation, i.e., activating only fibers innervating target muscles while avoiding off-target recruitment. Selectivity depends strongly on the electrode design. Extraneural interfaces, such as cuff electrodes [11], offer less invasive solutions, whereas intraneural electrodes, including longitudinal intrafascicular electrodes (LIFE) [12], transverse intrafascicular multichannel electrode (TIME) [13], and the Utah slanted electrode array (USEA) [14] penetrate the nerve to improve selectivity at the cost of increased invasiveness [15], [16]. These technologies have enabled restoration of hand opening/closing [6], [7], reaching and grasping [7], [8], [9], and even individual digit movements [17].

Despite these advances, stimulation protocols are still largely tuned empirically, requiring time and often yielding suboptimal results. Automating this process is essential for broader clinical adoption. Computational models offer a framework for optimizing stimulation [18], [19], [20], but their effectiveness depends on knowledge of the subject-specific internal organization of the nerve [8], [21]. Generic or average models can provide useful guidelines (e.g., benefits of current steering [22], [23] or intraneural interfaces [24]) but cannot directly produce patient-specific protocols.

This limitation is compounded by the complex and highly variable cross-sectional organization of peripheral nerves, where motor axons targeting different muscles are distributed across multiple fascicles in patterns that vary across individuals and along the nerve [21], [25], [26]. Imaging techniques such as high-field MRI and ultrasonography can resolve fascicular anatomy [27], [28] but do not provide muscle-specific functional information. Traditional methods to identify functional organization, such as immunohistochemistry [29], [30] and retrograde tracing [31], [32], [33] , are not applicable *in vivo* in humans. Electrical impedance tomography (EIT) has been proposed to map neural activity by detecting small impedance changes, potentially localizing active regions within a nerve [34], [35]. However, EIT provides only low-resolution spatial information, requires either residual activity or evoked responses, and depends on specialized hardware to measure very small signals, limiting its clinical applicability.

Here, we propose INFORM (Inference of Neural Functional Organization from Recruitment Matching), a framework to infer nerve functional organization directly from standard calibration data of implanted PNS systems. INFORM leverages monopolar recruitment curves (RCs), obtained by recording surface EMG during amplitude sweeps, which are routinely acquired in clinical practice. The method uses Bayesian optimization to calibrate a biophysically grounded neuroelectric model of the implanted nerve and then exploits this model to design selective stimulation protocols through model-based optimization, accelerated by machine learning approximations of fiber activation. In this work, we investigate whether muscle-specific functional organization can be reliably inferred from stimulation data alone, enabling patient-specific optimization without direct anatomical knowledge.

Results

In the following, we present a series of computational experiments designed to evaluate the proposed localization algorithm. Specifically, we aim to demonstrate that the algorithm accurately recovers the spatial organization of fiber clusters, and that the inferred organization can be leveraged to optimize selective stimulation protocols.

A nerve cross-section is described in terms of both its structural and functional organization. The structural component is defined by the positions and radii of its fascicles. The functional component is given by the identities and spatial distributions of the fibers within the section. Fibers innervating a given muscle are modeled as Gaussian clusters, parameterized by a center and dispersion, to approximate the somatotopic organization commonly assumed in peripheral nerves [19], [36], [37], [38]. Two TIMEs are inserted into the cross-section and modeled as point current sources. RCs are then simulated for each fiber cluster, defined as the proportion of activated fibers within the cluster as a function of stimulation amplitude (**Figure 1A**, **Methods – *In silico nerve sections*** and ***Neuroelectric "hybrid" models of electrical stimulation***).

Following the structure of the localization algorithm, and given a hypothesized nerve anatomy, the spatial distribution of each fiber cluster is inferred via Bayesian optimization. The optimization targets the parameters of each Gaussian cluster (center and dispersion) by minimizing the discrepancy between RCs generated from the original nerve section and those produced by candidate functional organizations. Notably, the structural model used during localization may differ from the original nerve structure, thereby explicitly accounting for uncertainty in the internal anatomy (**Figure 1B, Methods – *Localization algorithm***).

Finally, we address the optimization of stimulation protocols based on the assumed nerve structure and the inferred functional organization. Optimal protocols maximize selectivity within the inferred model. To obtain a more realistic estimate of performance, these optimized protocols are subsequently applied to the original nerve model, allowing assessment of their true selectivity under structural mismatch (**Figure 1C, Methods – *Stimulation protocol optimization***).

Our method correctly localizes fiber clusters when nerve structure is given

Figure 2 illustrates the performance of the proposed localization algorithm under the assumption that the nerve structure is known. In **Figure 2A–C**, we provide a detailed analysis for a representative nerve section. A visual comparison between the true and inferred functional organizations reveals a close correspondence, with fibers innervating the same muscles occupying similar spatial regions (**Figure 2A**). The inferred RCs show strong agreement with the ground truth across stimulation sites (**Figure 2C**), accurately capturing both thresholds and saturation behavior. Localized discrepancies are nevertheless observed for cluster 3, where a moderate error in the estimated dispersion leads to a more confined spatial distribution relative to the underlying fascicular geometry. Despite this, the overall recruitment behavior remains well approximated.

To quantitatively assess performance, we evaluated localization and recruitment errors across 50 functional organizations for each of the nerve structures shown in **Figure 2D**. Additional examples for nerves 2 and 3 are provided in **Supplementary Figures 1–2.** Across all nerves, the distance between true and inferred cluster centers remained consistently low, with the majority of values below 0.5 mm (**Figure 2E**). Median center localization errors were 0.34 mm (IQR: 0.21–0.43 mm) for nerve 1, 0.29 mm (0.18–0.42 mm) for nerve 2, and 0.29 mm (0.20–0.43 mm) for nerve 3. The relative error in cluster dispersion was generally below 50% (**Figure 2F**), although with greater variability compared to center estimates. Median relative dispersion errors were 37.6% (IQR: 20.1–50.8%) for nerve 1, 31.0% (12.9–47.0%) for nerve 2, and 31.5% (15.9–47.3%) for nerve 3. Recruitment errors (**Figure 2G**) were typically below 20 μA, corresponding to approximately 2% of the explored current range, indicating a limited impact on activation predictions. Consistently, recruitment-current RMSE values at the I50 condition remained low across all nerves, reaching 0.047 mA for nerve 1, 0.049 mA for nerve 2, and 0.071 mA for nerve 3, with most error distributions confined within approximately ±0.05–0.1 mA.

The behavior of the optimization underlying these results is reported in **Figure 3**. In the two representative populations shown in **Figure 3A**, the candidates queried by the algorithm progressively concentrated within a limited region of the cross-section, while for clusters 2–4 the prior inherited from the previously optimized clusters already covered the section with informative objective values. Pooling all candidates evaluated across the four clusters and the 50 populations (**Figure 3B**), the objective function decreased markedly with the distance between a candidate and the final best estimate of its cluster along both spatial coordinates, from approximately −0.044 at the best estimate to approximately −0.24 at a distance of 5 mm, whereas it remained essentially constant over the entire explored range of dispersion (total variation of 0.023, against 0.239 and 0.219 for the two spatial coordinates). The objective function is therefore dominated by the spatial position of the cluster and only weakly sensitive to its dispersion, consistent with the larger and more variable relative errors observed for cluster dispersion than for cluster centers (**Figure 2E–F**).

Convergence required 9.5 ± 5.0 iterations for cluster 1 and substantially fewer iterations for the following clusters, namely 4.6 ± 3.1, 4.7 ± 4.1 and 2.6 ± 1.8 iterations for clusters 2, 3 and 4,

corresponding to 21.4 ± 8.1 iterations per population overall (**Figure 3C**). This reduction reflects the sequential warm-start of the Gaussian Process, as each cluster after the first inherits all candidates already evaluated and therefore begins its optimization with an informed prior over the parameter space. Consistently, the median maximum Expected Improvement (**Methods – *Localization algorithm***) of clusters 2–4 fell below the stopping threshold within the first two to four iterations, while cluster 1 required approximately nine iterations (**Figure 3D**). Accordingly, the low-EI criterion terminated 43 out of 50 runs for cluster 1 and 49, 49 and 50 runs for clusters 2, 3 and 4 respectively, with the remaining runs stopping at the maximum iteration limit; no run terminated because the best objective value remained unchanged for 15 consecutive iterations. Termination was thus almost always driven by exhaustion of the expected improvement rather than by the iteration cap. Despite the different number of iterations, the final objective value was comparable across clusters, with medians of −0.0017, −0.0014, −0.0016 and −0.0015 for clusters 1–4, and for cluster 1 the runs that reached the iteration limit achieved final objective values overlapping with those of the runs that converged through the EI threshold (median −0.0019, IQR −0.0047 to −0.0018, n = 7, versus −0.0015, IQR −0.0025 to −0.0010, n = 43). The iteration cap therefore does not appear to limit the quality of the reconstruction.

Fiber cluster localization enables stimulation protocol optimization

We then assessed whether stimulation protocols optimized on the inferred functional organization could achieve, when applied to the true organization, a level of selectivity comparable to that obtained by protocols optimized directly on the true organization. A representative example is shown in **Figure 4A–C**. **Figure 4A** reports the true and inferred functional organizations used as reference for the analyses shown in **Figure 4B–C**. As shown in **Figure 4B**, stimulation protocols optimized on the true and inferred organizations generally employed the same dominant cathodic stimulation site, whereas anodic site position and amplitude were more variable. Despite these differences, the resulting recruitment patterns remained largely consistent across most clusters. The largest discrepancy was observed for cluster 2, where the protocol optimized on the true organization recruited a small proportion of non-target fibers (**Figure 4B**), resulting in lower selectivity compared to the protocol optimized directly on the inferred organization (**Figure 4C**). In contrast, clusters 1, 3, and 4 showed close agreement in both recruitment behavior and selectivity values between the two optimization strategies.

Figure 4D summarizes selectivity mismatches across the 150 automatically generated nerve sections (50 per nerve structure), corresponding to the localization results shown in **Figure 2E–G**. Selectivity differences remained strongly concentrated around zero, with median mismatches of −0.009 for nerve 1, −0.003 for nerve 2, and −0.020 for nerve 3. Interquartile ranges remained narrow, extending from −0.025 to 0.000 for nerve 1, from −0.027 to 0.000 for nerve 2, and from −0.073 to −0.005 for nerve 3, indicating very good agreement between protocols optimized on the true and inferred organizations. Values exceeding an absolute mismatch of 0.2 were uncommon, although occasional outliers were observed, particularly for nerve 3. Overall, the distributions were slightly shifted toward negative values, indicating that

optimization performed directly on the true organization generally yielded slightly higher selectivity values than optimization performed on the inferred organization.

Localization and optimization algorithms are robust to uncertainties in structure

Figure 5 shows the performance of the localization algorithm when the implanted nerve structure is perturbed by random fascicle shifts and resizing, modelling uncertainty in the target anatomy (see **Methods – *In silico* nerve sections**). In **Figure 5A**, we present an example comparing the nerve structure used to generate the reference RCs with the modified structure used in the localization algorithm, along with the corresponding localization errors (**Figure 5B**) and errors in the inferred RCs (**Figure 5C**).

The inferred functional organization preserved the spatial segregation of fiber clusters, although cluster dispersion was more variable compared to the true-structure case. The inferred RC aligned well with the true RC for clusters 1 and 2, while larger discrepancies were observed for clusters 3 and 4 (**Figure 5C**). In particular, cluster 4 exhibited a step-like recruitment pattern at sites 3 and 6, indicating sequential activation of spatially separated fiber clusters, a feature not present in the true RC. Representative examples of RC reconstruction for one population in nerves 2 and 3 are also reported in **Supplementary Figures 3 and 4**.

Across 50 populations per nerve (**Figure 5D**), the center distance error increased compared to the true-structure case, although median localization errors remained below 0.4 mm across all nerves. Median center localization errors were 0.36 mm (IQR: 0.23–0.53 mm) for nerve 1, 0.27 mm (0.18–0.39 mm) for nerve 2, and 0.33 mm (0.22–0.45 mm) for nerve 3, with distributions extending toward higher values under structural mismatch. The relative standard error in cluster dispersion showed broader distributions compared to the exact-structure condition, with median values of 33.4% (IQR: 16.5–46.7%) for nerve 1, 30.7% (16.7–44.8%) for nerve 2, and 30.3% (16.7–47.9%) for nerve 3, and some values approaching ~100%. Despite these increases in localization error, recruitment inferred errors remained centered around zero, indicating that overall recruitment behavior was still largely preserved. Recruitment-current RMSE values at the I50 condition increased to 0.098 mA for nerve 1, 0.062 mA for nerve 2, and 0.071 mA for nerve 3, while most error distributions remained confined within approximately ±0.05–0.1 mA.

Figure 6 summarizes the selectivity results across the three nerves and 50 populations per nerve, reported as the difference between true-based and inferred-based selectivity, both evaluated on the true organization. Compared to the exact-structure condition (**Figure 4D**), the distributions became broader and shifted further toward negative values, particularly for shifted nerve 1. Median selectivity differences were −0.093 for shifted nerve 1, −0.015 for shifted nerve 2, and −0.026 for shifted nerve 3, indicating a larger reduction in selectivity when stimulation protocols were optimized on inferred organizations generated from inaccurate structural models. Interquartile ranges also increased substantially, especially for shifted nerve 1, where values extended from −0.199 to −0.005. Shifted nerve 2 and shifted nerve 3 showed narrower but still asymmetric distributions, with interquartile ranges of −0.079 to 0.000 and −0.070 to −0.005, respectively. Negative tails extended down to approximately −0.35, −0.18,

and −0.16 at the whisker limits for nerves 1–3, with occasional outliers reaching values below −0.5. Nevertheless, positive selectivity differences were also observed, reaching approximately +0.22 in some cases, indicating that inferred-based optimization could still occasionally achieve selectivity comparable to, or higher than, true-based optimization.

Localization enables optimization of stimulation protocols in a complex nerve

We further evaluated the localization algorithm on a median nerve model comprising 12 fiber clusters corresponding to anatomically defined muscle groups (**Figure 7A**). Two inferred structures were considered: one matching the true nerve structure and one with inexact structure generated through fascicle perturbation.

In both cases, the inferred RCs closely matched the true RC across stimulation sites (**Figure 7B**). For the majority of clusters, the inferred and true curves overlapped over most of the stimulation range, with differences generally limited to small shifts in activation threshold and slight variations in the steepness of the curves. In the inexact structural model, these discrepancies became more apparent for clusters spanning multiple fascicles, like in the case of cluster PQ, where inferred RC showed delayed recruitment onset and smoother transitions compared to the sharper recruitment observed in the true RC.

Selectivity optimization results (**Figure 7C**) further confirmed the robustness of the approach. Selectivity values computed on the true nerve using stimulation protocols optimized on the inferred organizations were comparable to those obtained using true-based optimization across most muscle groups. For several muscles (e.g., FDS, 2L, 1L, FPB, APB, OP), selectivity values remained high (approximately ≥0.8) and showed minimal differences between conditions. For other muscles (e.g., FCR, FPL, PQ, FDP), selectivity values were lower overall (approximately 0.4–0.7) but remained consistent between true-based and inferred-based protocols. Larger deviations were observed for a limited subset of muscles in the inexact structural case. In particular, muscles such as PL and PT showed noticeable reductions in selectivity when using inferred-based stimulation protocols, with decreases on the order of ~0.1–0.3 compared to true-based optimization. These reductions are consistent with the increased structural mismatch affecting clusters distributed across multiple or distorted fascicles (**Figure 7B**). Despite this, inferred-based selectivity remained within a comparable range for all muscles, and no systematic collapse in selectivity was observed.

Discussion

In this work, we investigate whether the localization of muscle-specific fiber clusters in an implanted nerve section can be inferred from stimulation data using a neuroelectric “hybrid” model of the nerve. The hybrid model was combined with an iterative, error-driven optimization procedure that localizes muscle-specific fiber clusters by minimizing the discrepancy between inferred and target monopolar RCs. We evaluated the performance of our localization framework on a simplified circular-fascicled nerve, and a median nerve model with realistic anatomy derived from histological cross-sections (**Figure 2**, **Figure 7**), and we characterized the behavior of the underlying Bayesian optimization (**Figure 3**). To evaluate robustness of our approach

we added a structural mismatch between inferred and target nerves consisting of shifted and reshaped fascicular geometries (**Figure 5**, **Figure 7**). Despite these structural differences, the inferred functional organizations consistently preserved the spatial segregation of muscle-specific fiber clusters. Furthermore, stimulation protocols optimized on the inferred nerves achieved selectivity levels on the true nerve that were comparable to those obtained when optimizing directly on the true functional organization (**Figure 4D**, **Figure 7C**), with only limited degradation under inexact structural assumptions (**Figure 6**, **Figure 7C**). Together, these results indicate that RCs alone can provide sufficient information to infer the functional organization of peripheral nerves, even in the absence of subject-specific anatomical knowledge. This supports the feasibility of fast, robust, and clinically viable approaches for the design of selective stimulation protocols and the personalization of peripheral nerve stimulation strategies for motor restoration.

Compared with existing approaches, INFORM differs fundamentally in that it does not rely on direct imaging or invasive tracing techniques to recover functional organization. High-field MRI and ultrasonography resolve fascicular anatomy but carry no muscle-specific functional labeling [27], [28]; immunohistochemistry and retrograde tracing provide that labeling but are not applicable *in vivo* in humans [29], [31], [32]; and EIT, while able to localize neural activity, offers limited spatial resolution, requires residual or evoked activity, and depends on specialized hardware to resolve very small impedance changes [34], [35]. In contrast, INFORM leverages standard calibration data already available in clinical workflows, directly linking inferred structure to muscle-level function and enabling immediate use for stimulation optimization. It also differs from purely empirical protocol tuning, which is restricted to the protocols that can be tested on the subject, whereas an explicit model allows a far larger protocol space to be searched offline.

Importantly, our results highlight that accurate reconstruction of exact anatomical organization is not strictly necessary to achieve high selectivity. Even when the inferred organization deviates from the true underlying structure, the resulting stimulation protocols remain highly effective. This suggests that the optimization process primarily requires a functionally consistent representation of the nerve, rather than a fully anatomically correct one, which substantially relaxes the requirements for patient-specific modeling, because it shifts the target of inference from anatomy, which is difficult to obtain *in vivo*, to input–output behavior, which is directly measurable.

Characterizing the optimization landscape clarified which properties of a fiber cluster are actually recoverable from RCs (**Figure 3B**). Pooling all evaluated candidates, the objective function varied by 0.22 to 0.24 across the explored range of each spatial coordinate, but by only 0.023 across the explored range of dispersion, an order of magnitude less. Cluster position is thus strongly constrained by the data, whereas dispersion is nearly unconstrained. This asymmetry accounts for the pattern of errors in **Figure 2E–F**, where median center errors remained below 0.35 mm while relative dispersion errors were 31 to 38% and considerably more variable, and it suggests that the framework is best interpreted as a localizer of cluster position rather than as a full characterization of cluster shape. It also helps explain why selectivity is largely

preserved: current steering depends primarily on where a target population lies relative to the active sites, which is the property the data constrain best, and only weakly on how tightly that population is packed. Consistently, protocols optimized on the true and the inferred organization converged on the same dominant cathodic site, differing mainly in anodic position and amplitude (**Figure 4B)**. Median selectivity mismatches were −0.009, −0.003 and −0.020 across the three structures, with interquartile ranges under 0.03 (**Figure 4D**). Selectivity is governed principally by where current is steered, the property the data constrain best, and only weakly by the anodic detail.

The median nerve model shows that the approach scales from four to twelve clusters and that its failures are anatomically interpretable (**Figure 7**). Inferred RCs matched the true ones across stimulation sites under both structural conditions, and selectivity on the true nerve was comparable between true-based and inferred-based protocols for most muscles. The relatively low selectivity values reported for some of the targeted muscles are in general coherent with an implant in the main trunk of the median nerve with respect to a more distal implant [39], or to several implants in different distal branches [17]. Moreover, we highlight that it is still possible that such neural selectivity values may lead to functional and even kinematically selective movements as we have shown adding musculoskeletal modelling in cascade to neuroelectric modelling in [17].

In a realistic clinical scenario, the inference process would need to operate under additional sources of variability, including measurement noise, limited sampling of stimulation conditions, and uncertainty in electrode positioning. These factors could be mitigated by incorporating additional constraints into the model, such as anatomical priors on fascicle size and distribution, regularization of spatial organization, or probabilistic formulations that explicitly account for uncertainty. Integrating complementary data sources, when available, could further refine the inferred solutions without being strictly required.

Future work should extend the framework to systematically compare different electrode designs and configurations, including extraneural and intraneural interfaces, to assess how the richness of stimulation patterns affects identifiability and optimization performance. Moreover, expanding the approach to spatiotemporal stimulation strategies could further improve selectivity and functional outcomes.

Finally, a key limitation of this study is that validation was performed entirely *in silico*. Real EMG recordings are subject to noise, cross-talk, and variability in electrode placement, which may impact the quality of the inferred RCs. Therefore, experimental validation *in vivo* will be essential to assess the robustness and practical applicability of the approach. Demonstrating reliable performance under realistic clinical conditions will be a critical step toward translating INFORM into a deployable tool for neuroprosthetic applications. To support independent validation and reuse, all data and code necessary to replicate the main results of this study are made openly available (see **Data and Code Availability**).

Methods

In silico nerve sections

Circular simplified nerve sections

Structure. We generated three synthetic nerve cross-sectional structures, each consisting of a circular epineurium with a diameter of 3 mm. For each structure, the fascicular organization was defined by nine circular fascicles, whose diameters were independently sampled from a uniform distribution between 0.3 and 0.7 mm.

To simulate structural uncertainty, we generated one perturbed version of each nerve structure. Fascicles were perturbed sequentially in a randomly assigned order. For each fascicle, both its center position and radius were modified, and the perturbation was accepted only if it did not introduce intersections with other fascicles. Specifically, the fascicle center was displaced independently along the x- and y-axes by values sampled from a uniform distribution between −0.1 and 0.1 mm. The fascicle radius was then scaled by a factor corresponding to a relative change sampled uniformly between −20% and +20%.

Functional organization. Each nerve section was assigned four functional fiber clusters. First, 400 candidate fiber locations were sampled uniformly within each fascicle, defining the full set of available fibers across the nerve section. For each cluster, the cluster center was sampled uniformly within one fascicle, and the spatial dispersion was sampled uniformly between 0.15 and 0.5 mm. Cluster membership was then generated by selecting 200 fibers from the full candidate fiber set, with selection probabilities decreasing with distance from the cluster center and controlled by the sampled dispersion. Thus, each functional cluster corresponded to a spatially localized subset of the available intrafascicular fibers, while allowing cluster membership to be defined over the entire nerve cross-section.

Electrode placement. Stimulation sites were arranged on a regular 5 × 5 grid inscribed within a square region whose diagonal matched the nerve cross-sectional diameter (6 mm). From this grid, only the two diagonals were retained, defining two cross-shaped transverse intrafascicular multichannel electrode (TIME) configurations used in the subsequent analyses.

Median nerve sections

Structure. In this example, true structural and functional organizations were adapted from a previously published work [40], and consists of detailed fascicular reconstructions of the human median nerve derived from manual segmentation of stained histological cross sections obtained from a human cadaver [41]. The nerve was partitioned into 12 consecutive blocks spanning from the styloid process to approximately 30% of the distance toward the elbow. In this work, we selected block 10, corresponding to a proximal location above the elbow, where fascicles containing fibers for all muscles innervated by the median nerve are still present. The selected nerve cross-section had a major semi-axis of approximately 3 mm and contained 16 fascicles, with major and minor semi-axes ranging from 0.146 to 0.555 mm and from 0.111 to 0.440 mm, respectively.

Electrode placement. To simulate structural uncertainty, we generated one perturbed version of the median nerve structure, following the same procedure adopted for the circular simplified nerve sections. For each fascicle, both its center position and radius were modified, and the perturbation was accepted only if it did not introduce intersections with other fascicles. Specifically, the fascicle center was displaced independently along the x- and y-axes by values sampled from a uniform distribution between −0.1 and 0.1 mm. The fascicle radius was then scaled by a factor corresponding to a relative change sampled uniformly between −20% and +20%. The considered median nerve cross-section had a maximum radius of approximately 3 mm.

Functional organization. To model the functional organization of the nerve, 12 muscle groups were defined according to the known innervation targets of the median nerve: opponens pollicis (OP), abductor pollicis brevis (APB), flexor pollicis brevis (FPB), first and second lumbricals (1L, 2L), flexor digitorum superficialis (FDS), pronator quadratus (PQ), flexor digitorum profundus (FDP), flexor pollicis longus (FPL), palmaris longus (PL), flexor carpi radialis (FCR), and pronator teres (PT). Following the approach adopted in [40],5,000 fibers were uniformly distributed across all fascicles. Fiber-to-muscle assignments were then generated using probabilistic sampling from two-dimensional Gaussian distributions centered at predefined locations, thereby approximating the functional organization of fibers within the nerve. Each cluster was composed of 200 fibers. Additional methodological details are available in [40].

For the median nerve section, stimulation sites were first generated on a regular 5 × 5 grid with 1 mm spacing covering the entire nerve cross-sectional area. Only the sites located within the nerve boundary were retained. From these candidate locations, two cross-shaped TIME configurations were manually selected for the subsequent analyses.

Neuroelectric “hybrid” model of PNS

Volume conduction

A computational model of electrical stimulation was implemented using the hybrid modeling framework described in [38]. Nerve geometries were generated by extruding the previously defined true and inferred transverse sections over a 2 cm longitudinal segment. Point current sources were positioned at the designated electrode sites to represent stimulation locations. To emulate the surrounding biological environment, nerves were embedded in a cylindrical saline bath with a 10 mm radius, with the outer boundary maintained at 0 V to serve as ground. The resulting electric field was calculated under the quasistatic approximation by solving the Laplace equation [42], [43]. Tissue conductivities were assigned as follows: extra-fascicular epineurium ($\sigma_x = \sigma_y = \sigma_z = 0.083\ \mathrm{S/m}$), fascicular endoneurium ($\sigma_x = 0.571, \sigma_y = \sigma_z = 0.083\ \mathrm{S/m}$), perineurium ($\sigma_x = \sigma_y = \sigma_z = 0.0009\ \mathrm{S/m}$), and saline ($\sigma_x = \sigma_y = \sigma_z = 2\ \mathrm{S/m}$) [38], [44]. The perineurium was modeled as a thin resistive layer with a thickness equal to 3% of the corresponding fascicle diameter [45]. The subset of fibers belonging to the extracted functional clusters was used for subsequent finite element simulations. Finite element simulations were conducted separately for each stimulation site, applying 1 μA of current while

leaving all other sites inactive. The resulting extracellular potentials were interpolated using COMSOL 6.1 and assembled into a lead-field matrix (LFM) [38], which maps the sensitivity values of the currents injected at each electrode to the extracellular potentials at each node along the modeled fibers. Potentials outside the modeled domain were set to zero.

Neural response computation

Neural activation was simulated using multicompartment models of myelinated human motor fibers in NEURON 8.2.2. We adopted the Gaines et al. adaptation [46] of the McIntyre-Richardson-Grill (MRG) model [47]. Fibers were modeled with 40 internodes and 41 nodes of Ranvier, with diameters uniformly sampled between 12–20 μm (Aα range). Axons were assumed straight and longitudinally aligned within the nerve, with transverse positions assigned randomly within their respective fascicles.

Action potentials were identified as peaks in the membrane potential at the recording node of stimulated fibers and detected using the scipy.signal.find_peaks Python function, with a minimum height of 0 mV and a minimum prominence of 60 mV [40]. This criterion corresponds to peaks that are at least 0 mV in absolute value and at least 60 mV above the resting potential. A fiber was considered active if it exhibited at least one action potential during the simulation period.

Surrogate models of fiber activation

Following the methodology established in our previous work [40], [48], we developed machine-learning surrogate models to accelerate neural activation predictions. Training data were generated using our hybrid computational models by random sampling a nerve fiber, an electrode active site positioning, and a stimulation current amplitude between 0-1000 μA. For each training sample, we applied a biphasic cathodic-first pulse with 500 μs pulse width, applied 10 ms after the start of the simulation, and lasting a total of 50 ms. We then assigned binary labels based on whether fiber activation was achieved. Feature extraction included fiber diameter measurements and extracellular potential recordings at Ranvier nodes during the cathodic phase of stimulation. We constructed individual training datasets for each employed nerve section, with each dataset comprising 10,000 samples. XGBoost classifiers were implemented using the XGBClassifier class from the xgboost.sklearn module, default hyperparameter configurations for each section-specific dataset.

Recruitment curve computation

For a given fiber cluster *c* and stimulation protocol *s*, the recruitment value $\mu_{c,s}$ was quantified as the fraction of fibers within the cluster that were activated:

$$\mu_{c,s} = n_{c,s}^{act}/n_c,$$

where $n_{c,s}^{act}$ is the number of activated fibers in fiber cluster c and n_c is the total number of fibers in that cluster ($n_c = 200$). Monopolar RCs were then constructed by collecting 20 recruitment values obtained at evenly spaced current amplitudes ranging from 0 to 1 mA.

Localization algorithm

The localization problem consisted in assigning fibers of a nerve model with defined anatomical structure to specific functional clusters, in order to reconstruct its functional organization. This was achieved through a Bayesian optimization framework that, for each functional cluster, identified the optimal spatial allocation of fibers within the nerve structure. Each allocation was parametrized by the cluster center coordinates and standard deviation, assuming a Gaussian spatial distribution of fiber membership around the cluster center. The optimization minimized the discrepancy between the RCs generated by the reconstructed model and those of a reference nerve model with known structure and functional organization (**Figure 1B**). While in this work both the reference and inferred nerves are computational, allowing direct validation against a ground truth, the framework is designed to generalize to experimental settings, where only the RCs of the reference nerve would be available from electrophysiological recordings, without any prior knowledge of the underlying functional organization.

Candidate cluster configurations were defined over a four-dimensional parameter space, constructed as the Cartesian product of uniformly sampled values for each parameter. The parameters consisted of a spatial location (x, y), indicating the center of the cluster, standard deviation σ, indicating the dispersion, and a numerical parameter n, indicating the number of fibers within the cluster. The spatial location (x, y) was initially defined over a square region $[-R, R] \times [-R, R]$ with $R = 3mm$ corresponding to the nerve radius, discretized uniformly with 20 points per dimension, resulting in a spatial resolution of approximately 0.3 mm. The standard deviation σ was uniformly sampled in the interval ([0.15–0.5] mm for circular nerves, consistent with the dispersion range used during the generation of the synthetic functional clusters. For the segmented median nerve, σ was sampled in the interval [0.05, 0.2] mm , following the range adopted in the previously published study [40]. In both cases,20 equally spaced points were considered (step ≈ 0.0079). The fiber count *n* was fixed at 200 for all candidates; while the optimization framework supports treating n as a free parameter, a constant value was adopted here to reduce the search space, as the number of fibers per cluster was not the target of the localization. The full candidate space resulted in 8,000 unique candidate configurations. A geometric constraint was then applied by retaining only candidates whose center fell within the nerve cross-section ($\sqrt{x^2 + y^2} < R$), reducing the valid set to 5,520 candidates. Prior to optimization, all candidate parameters were standardized using z-score normalization (*StandardScaler* from *sklearn.preprocessing),* to improve numerical stability of the Gaussian Process.

Localization was formulated as a sequential Bayesian optimization problem and implemented using the modAL package in Python [49]. A Gaussian Process (GP) regressor (*GaussianProcessRegressor* from *sklearn.gaussian_process*) with a Matérn 5/2 kernel was used to model the relationship between candidate cluster parameters and the objective function. The objective function was defined as the negative mean squared error (MSE) between the RCs of the reference cluster and those generated by a candidate configuration,

computed across all stimulation sites and stimulation amplitudes, and was maximized by the optimizer. The kernel was initialized with unit length scales across all four input dimensions and evolved according to collected observations during each iteration. The exploration–exploitation trade-off was controlled by a tradeoff parameter tr = 0.01 in the Expected Improvement (EI) acquisition function. Optimization proceeded sequentially across the four functional clusters. For the first cluster, the GP was initialized by randomly sampling 30 candidate configurations from the standardized grid to establish an initial prior. For each following cluster, the GP was instead pre-trained using all candidate configurations and their associated RCs already evaluated during the optimization of the preceding clusters, recomputing the corresponding objective values against the new cluster's reference curves. This warm-start strategy avoided redundant simulations and allowed the GP to begin each cluster optimization with an informed prior over the parameter space. At each iteration the next candidate was selected by maximizing the EI acquisition function over all valid standardized candidates (*max_EI* from *modAL.acquisition*). The RCs for the selected candidate were generated using the electrical stimulation model described above. Optimization was terminated early if any of the following conditions was met: (i) the maximum EI across all candidates fell below a threshold (1×10^{-8}), indicating that further exploration was uninformative; (ii) the best observed objective value remained unchanged for 15 consecutive iterations, indicating convergence; or (iii) a maximum of 20 iterations was reached. The final estimate for each cluster corresponded to the candidate yielding the highest posterior objective value, defined by the cluster center coordinates and spatial standard deviation. This procedure was repeated independently for all four clusters, yielding an inferred nerve model comprising four localized functional clusters.

Spatial errors of localization

Localization accuracy was quantified by comparing inferred cluster parameters with ground-truth parameters extracted from the true nerve. For each cluster, spatial error was computed as the Euclidean distance between the inferred cluster center $(x_{\text{pred}}, y_{\text{pred}})$ and the true cluster center $(x_{\text{ref}}, y_{\text{ref}})$. Relative errors were computed for cluster standard deviation as the absolute difference between inferred and true values normalized by the true.

To account for biases introduced by discretization and non-uniform fiber distributions within clusters, corrected reference parameters were also computed directly from individual fiber locations. Specifically, corrected cluster centers were obtained as the means of the fiber coordinates belonging to each cluster, and corrected cluster dispersion was computed as the standard deviation of the radial distance of fibers from the nerve center. Localization errors were then recomputed using these corrected reference values, yielding corrected spatial and dispersion errors.

Stimulation protocol optimization

To assess the accuracy of the inferred functional organizations, the stimulation protocol maximizing the selectivity of each fiber cluster was optimized independently on both the true and inferred nerve sections. The resulting optimal stimulation protocols were then evaluated on the true nerve section, and the outcomes were compared. Optimization on the true nerve

section was performed as a hypothetical reference case, aimed at estimating the selectivity that would be achieved if the real nerve geometry were available for optimization. *Inferred - based selectivity* was defined as the selectivity obtained using the protocol optimized on the inferred section, whereas *true-based selectivity* referred to the selectivity obtained using the protocol optimized on the true section.

Selectivity metrics

As shown in our previous work [50], the choice of selectivity metric used to guide the optimization function can strongly influence the results. However, the optimal objective function is not immediately the best metric to interpret them. For this reason, we employed two different selectivity metrics for optimization and for evaluating the outcomes.

For a given fiber cluster *c* and stimulation protocol *s*, with recruitment value $\mu_{g,s}$, the optimization was guided by the selectivity metric $Sel_{c,s}^{OPT}$, defined as

$$Sel_{c,s}^{OPT} = \frac{\mu_{c,s}^2}{\sum_{c'=1}^{C} \mu_{c',s}},$$

where C is the total number of fiber clusters. On the other hand, to assess the effectiveness of the resulting stimulation protocols, we employed the metric $Sel_{c,s}^{EVAL}$ introduced in [19]:

$$Sel_{c,s}^{EVAL} = \mu_{c,s} - \frac{1}{C-1} \sum_{c'=1, c' \neq c}^{C} \mu_{c',s},$$

Optimization strategy

To determine stimulation protocols that maximize selectivity for each fiber cluster in a population, a Particle Swarm Optimization (PSO) algorithm was applied, implemented via the GlobalBestPSO class from the PySwarms library in Python. The swarm consisted of 25 particles and was allowed to evolve for 50 iterations. Early stopping was applied if the best cost value changed by less than 1×10^{-10} for 50 consecutive iterations. The PSO hyperparameters were set as follows: cognitive coefficient $c_1 = 1.5$, social coefficient $c_2 = 1.5$, and inertia weight $w = 0.9$. Optimization was conducted independently for each fiber cluster, using $Sel_{c,s}^{OPT}$ as the objective function. The PSO search space was defined over 2xN dimensions, where N is the number of electrode sites, encoding both stimulation amplitude and a ranking weight for each site. At each iteration, only the three highest-ranked sites were assigned non-zero stimulation amplitudes, while the remaining sites were set to zero, effectively constraining the solution to protocols activating exactly three electrodes simultaneously. Stimulation amplitudes were bounded in the range [−1, 1] mA, while the ranking weights were bounded in [0, 1].

Data and Code Availability

All data and code necessary to replicate the main results of this study are openly available. The code is available on GitHub at https://github.com/LauraToni/INFORM , and the associated data are archived on Zenodo at https://doi.org/10.5281/zenodo.22229593.

Author Contributions

L.T. Conceptualization, Methodology, Software, Formal analysis, Investigation, Data Curation, Writing - Original Draft, Writing – Review & Editing, Visualization; **V.F.** Conceptualization, Methodology, Software, Investigation, Data Curation, Writing - Original Draft, Writing – Review & Editing; **C.V.** Methodology, Software, Writing – Review & Editing; **E.L.** Methodology, Software, Writing – Review & Editing; **S.M.** Resources, Writing – Review & Editing, Supervision, Funding acquisition; **S.R.** Conceptualization, Methodology, Software, Formal analysis, Writing - Original Draft, Writing – Review & Editing, Visualization, Supervision

Funding

This paper was partly funded by the Italian Ministry of University and Research (MUR) under the National Recovery and Resilience Plan (NRRP) for the MNESYS (PE0000006) and THE (IECS00000017) projects. And by the Swiss National Science Foundation (grants agreements 10·003·473 and 200021E_229225).

Declaration of Competing Interests

S.M. and S.R. are co-authors of a patent (WO2024095142A2) including the description of the localization method presented in this manuscript.

References

[1] Z. Gao *et al.*, «Restoring After Central Nervous System Injuries: Neural Mechanisms and Translational Applications of Motor Recovery», *Neurosci. Bull.*, vol. 38, fasc. 12, pp. 1569–1587, dic. 2022, doi: 10.1007/s12264-022-00959-x.

[2] P. Langhorne, J. Bernhardt, e G. Kwakkel, «Stroke rehabilitation», *The Lancet*, vol. 377, fasc. 9778, pp. 1693–1702, mag. 2011, doi: 10.1016/S0140-6736(11)60325-5.

[3] «Spinal Cord Injury Rehabilitation | F.A. Davis PT Collection | McGraw Hill Medical». Consultato: 29 maggio 2026. [Online]. Disponibile su: https://fadavispt.mhmedical.com/book.aspx?bookid=1947&isMissingChapter=true

[4] L. Boccuni, L. Marinelli, C. Trompetto, A. Pascual-Leone, e J. M. Tormos Muñoz, «Time to reconcile research findings and clinical practice on upper limb neurorehabilitation», *Front. Neurol.*, vol. 13, p. 939748, lug. 2022, doi: 10.3389/fneur.2022.939748.

[5] G. Kwakkel, B. J. Kollen, J. van der Grond, e A. J. H. Prevo, «Probability of Regaining Dexterity in the Flaccid Upper Limb», *Stroke*, vol. 34, fasc. 9, pp. 2181–2186, set. 2003, doi: 10.1161/01.STR.0000087172.16305.CD.

[6] X. Navarro, T. B. Krueger, N. Lago, S. Micera, T. Stieglitz, e P. Dario, «A critical review of interfaces with the peripheral nervous system for the control of neuroprostheses and hybrid bionic systems», *J. Peripher. Nerv. Syst.*, vol. 10, fasc. 3, pp. 229–258, 2005, doi: 10.1111/j.1085-9489.2005.10303.x.

[7] W. D. Memberg *et al.*, «Implanted neuroprosthesis for restoring arm and hand function in people with high level tetraplegia», *Arch. Phys. Med. Rehabil.*, vol. 95, fasc. 6, pp. 1201-1211.e1, giu. 2014, doi: 10.1016/j.apmr.2014.01.028.

[8] M. A. Schiefer *et al.*, «Selective activation of the human tibial and common peroneal nerves with a flat interface nerve electrode», *J. Neural Eng.*, vol. 10, fasc. 5, p. 056006, ago. 2013, doi: 10.1088/1741-2560/10/5/056006.

[9] Y. Zhou *et al.*, «Peripheral Electrical Stimulation on Motor Function and Activities of Daily Living After Stroke: A Systematic Review and Network Meta-analysis», *Arch. Phys. Med. Rehabil.*, vol. 106, fasc. 8, pp. 1258–1266, ago. 2025, doi: 10.1016/j.apmr.2025.01.466.

[10] G. S. Dhillon e K. W. Horch, «Direct neural sensory feedback and control of a prosthetic arm», *IEEE Trans. Neural Syst. Rehabil. Eng.*, vol. 13, fasc. 4, pp. 468–472, dic. 2005, doi: 10.1109/TNSRE.2005.856072.

[11] K. H. Polasek, H. A. Hoyen, M. W. Keith, R. F. Kirsch, e D. J. Tyler, «Stimulation Stability and Selectivity of Chronically Implanted Multicontact Nerve Cuff Electrodes in the Human Upper Extremity», *IEEE Trans. Neural Syst. Rehabil. Eng.*, vol. 17, fasc. 5, pp. 428–437, ott. 2009, doi: 10.1109/TNSRE.2009.2032603.

[12] S. Micera *et al.*, «On the use of longitudinal intrafascicular peripheral interfaces for the control of cybernetic hand prostheses in amputees», *IEEE Trans. Neural Syst. Rehabil. Eng. Publ. IEEE Eng. Med. Biol. Soc.*, vol. 16, fasc. 5, pp. 453–472, ott. 2008, doi: 10.1109/TNSRE.2008.2006207.

[13] T. Boretius *et al.*, «A transverse intrafascicular multichannel electrode (TIME) to interface with the peripheral nerve», *Biosens. Bioelectron.*, vol. 26, fasc. 1, pp. 62–69, set. 2010, doi: 10.1016/j.bios.2010.05.010.

[14] A. Branner, R. B. Stein, e R. A. Normann, «Selective stimulation of cat sciatic nerve using an array of varying-length microelectrodes», *J. Neurophysiol.*, vol. 85, fasc. 4, pp. 1585–1594, apr. 2001, doi: 10.1152/jn.2001.85.4.1585.

[15] S. Raspopovic *et al.*, «Restoring natural sensory feedback in real-time bidirectional hand prostheses», *Sci. Transl. Med.*, vol. 6, fasc. 222, p. 222ra19, feb. 2014, doi: 10.1126/scitranslmed.3006820.

[16] S. Wendelken *et al.*, «Restoration of motor control and proprioceptive and cutaneous sensation in humans with prior upper-limb amputation via multiple Utah Slanted Electrode Arrays (USEAs) implanted in residual peripheral arm nerves», *J. NeuroEngineering Rehabil.*, vol. 14, fasc. 1, Art. fasc. 1, nov. 2017, doi: 10.1186/s12984-017-0320-4.

[17] S. Micera *et al.*, «Targeted nerve stimulation restores single-finger movements in a person with tetraplegia», 17 marzo 2025, *Research Square*. doi: 10.21203/rs.3.rs-6188325/v1.

[18] J. Zariffa, M. Nagai, Z. Daskalakis, e M. Popovic, «Influence of the Number and Location of Recording Contacts on the Selectivity of a Nerve Cuff Electrode», *IEEE Trans. Neural Syst. Rehabil. Eng. Publ. IEEE Eng. Med. Biol. Soc.*, vol. 17, pp. 420–7, lug. 2009, doi: 10.1109/TNSRE.2009.2023301.

[19] S. Raspopovic, M. Capogrosso, e S. Micera, «A Computational Model for the Stimulation of Rat Sciatic Nerve Using a Transverse Intrafascicular Multichannel Electrode», *IEEE Trans. Neural Syst. Rehabil. Eng.*, vol. 19, fasc. 4, pp. 333–344, ago. 2011, doi: 10.1109/TNSRE.2011.2151878.

[20] A. Wongsarnpigoon e W. M. Grill, «Energy-efficient waveform shapes for neural stimulation revealed with a genetic algorithm», *J. Neural Eng.*, vol. 7, fasc. 4, p. 046009, giu. 2010, doi: 10.1088/1741-2560/7/4/046009.

[21] S. Sunderland, «THE INTRANEURAL TOPOGRAPHY OF THE RADIAL, MEDIAN AND ULNAR NERVES», *Brain*, 1945, doi: 10.1093/brain/68.4.243.

[22] K. E. I. Deurloo, J. Holsheimer, e H. B. K. Boom, «Transverse tripolar stimulation of peripheral nerve: a modelling study of spatial selectivity», *Med. Biol. Eng. Comput.*, vol. 36, fasc. 1, pp. 66–74, gen. 1998, doi: 10.1007/BF02522860.

[23] M. A. Schiefer, R. J. Triolo, e D. J. Tyler, «A Model of Selective Activation of the Femoral Nerve With a Flat Interface Nerve Electrode for a Lower Extremity Neuroprosthesis», *IEEE Trans. Neural Syst. Rehabil. Eng. Publ. IEEE Eng. Med. Biol. Soc.*, vol. 16, fasc. 2, pp. 195–204, apr. 2008, doi: 10.1109/TNSRE.2008.918425.

[24] J. Badia, T. Boretius, D. Andreu, C. Azevedo-Coste, T. Stieglitz, e X. Navarro, «Comparative analysis of transverse intrafascicular multichannel, longitudinal intrafascicular and multipolar cuff electrodes for the selective stimulation of nerve fascicles», *J. Neural Eng.*, vol. 8, fasc. 3, p. 036023, giu. 2011, doi: 10.1088/1741-2560/8/3/036023.

[25] K. Gustafson, G. Pinault, J. Neville, I. Syed, J. Jean-Claude, e R. Triolo, «Fascicular anatomy of human femoral nerve: Implications for neural prostheses using nerve cuff electrodes», *J. Rehabil. Res. Dev.*, vol. 46, pp. 973–84, gen. 2009, doi: 10.1682/JRRD.2008.08.0097.

[26] G. P. Watchmaker, C. A. Gumucio, R. E. Crandall, M. A. Vannier, e P. M. Weeks, «Fascicular topography of the median nerve: A computer based study to identify branching patterns», *J. Hand Surg.*, vol. 16, fasc. 1, pp. 53–59, gen. 1991, doi: 10.1016/S0363-5023(10)80013-9.

[27] A. Chhabra *et al.*, «MR Neurography: Past, Present, and Future», *Am. J. Roentgenol.*, vol. 197, fasc. 3, pp. 583–591, set. 2011, doi: 10.2214/AJR.10.6012.

[28] M. R. Nouh, H. M. Abdel-Naby, T. El Sakka, e M. El-Shafei, «Peripheral nerve ultrasound: a survival guide for the practicing radiologist with updates», *Ultrasound J.*, vol. 17, fasc. 1, p. 21, mar. 2025, doi: 10.1186/s13089-024-00387-0.

[29] T. M. E. Brushart, «Central course of digital axons within the median nerve of macaca mulatta», *J. Comp. Neurol.*, vol. 311, fasc. 2, pp. 197–209, 1991, doi: 10.1002/cne.903110203.

[30] D. Prodanov e H. K. P. Feirabend, «Morphometric analysis of the fiber populations of the rat sciatic nerve, its spinal roots, and its major branches», *J. Comp. Neurol.*, vol. 503, fasc. 1, pp. 85–100, lug. 2007, doi: 10.1002/cne.21375.

[31] M. Rigaud *et al.*, «Species and strain differences in rodent sciatic nerve anatomy: implications for studies of neuropathic pain», *Pain*, vol. 136, fasc. 1–2, pp. 188–201, mag. 2008, doi: 10.1016/j.pain.2008.01.016.

[32] T. M. Brushart e M. M. Mesulam, «Alteration in connections between muscle and anterior horn motoneurons after peripheral nerve repair», *Science*, vol. 208, fasc. 4444, pp. 603–605, mag. 1980, doi: 10.1126/science.7367884.

[33] A. W. English, G. Schwartz, W. Meador, M. J. Sabatier, e A. Mulligan, «Electrical stimulation promotes peripheral axon regeneration by enhanced neuronal neurotrophin signaling», *Dev. Neurobiol.*, vol. 67, fasc. 2, pp. 158–172, feb. 2007, doi: 10.1002/dneu.20339.

[34] K. Aristovich *et al.*, «Imaging fast neural traffic at fascicular level with electrical impedance tomography: proof of principle in rat sciatic nerve», *J. Neural Eng.*, vol. 15, fasc. 5, p. 056025, ago. 2018, doi: 10.1088/1741-2552/aad78e.

[35] J. Hope, F. Vanholsbeeck, e A. McDaid, «A model of electrical impedance tomography on peripheral nerves for a neural-prosthetic control interface», *Physiol. Meas.*, vol. 39, fasc. 4, p. 044002, apr. 2018, doi: 10.1088/1361-6579/aab73a.

[36] J. D. Stewart, «Peripheral nerve fascicles: Anatomy and clinical relevance», *Muscle Nerve*, vol. 28, fasc. 5, pp. 525–541, 2003, doi: 10.1002/mus.10454.

[37] P. Bäumer, M. Weiler, M. Bendszus, e M. Pham, «Somatotopic fascicular organization of the human sciatic nerve demonstrated by MR neurography», *Neurology*, vol. 84, fasc. 17, pp. 1782–1787, apr. 2015, doi: 10.1212/WNL.0000000000001526.

[38] S. Romeni, G. Valle, A. Mazzoni, e S. Micera, «Tutorial: a computational framework for the design and optimization of peripheral neural interfaces», *Nat. Protoc.*, vol. 15, fasc. 10, pp. 3129–3153, ott. 2020, doi: 10.1038/s41596-020-0377-6.

[39] M. Badi *et al.*, «Intrafascicular peripheral nerve stimulation produces fine functional hand movements in primates», *Sci. Transl. Med.*, vol. 13, fasc. 617, p. eabg6463, ott. 2021, doi: 10.1126/scitranslmed.abg6463.

[40] S. Romeni *et al.*, «Combining biophysical models and machine learning to optimize implant geometry and stimulation protocol for intraneural electrodes», *J. Neural Eng.*, vol. 20, fasc. 4, p. 046001, lug. 2023, doi: 10.1088/1741-2552/ace219.

[41] I. Delgado-Martínez, J. Badia, A. Pascual-Font, A. Rodríguez-Baeza, e X. Navarro, «Fascicular Topography of the Human Median Nerve for Neuroprosthetic Surgery», *Front. Neurosci.*, vol. 10, lug. 2016, doi: 10.3389/fnins.2016.00286.

[42] B. Wang *et al.*, «Quasistatic approximation in neuromodulation», *J. Neural Eng.*, vol. 21, fasc. 4, lug. 2024, doi: 10.1088/1741-2552/ad625e.

[43] C. A. Bossetti, M. J. Birdno, e W. M. Grill, «Analysis of the quasi-static approximation for calculating potentials generated by neural stimulation», *J. Neural Eng.*, vol. 5, fasc. 1, pp. 44–53, mar. 2008, doi: 10.1088/1741-2560/5/1/005.

[44] S. Raspopovic, F. M. Petrini, M. Zelechowski, e G. Valle, «Framework for the Development of Neuroprostheses: From Basic Understanding by Sciatic and Median Nerves Models to Bionic Legs and Hands», *Proc. IEEE*, vol. 105, fasc. 1, pp. 34–49, gen. 2017, doi: 10.1109/JPROC.2016.2600560.

[45] N. A. Pelot, C. E. Behrend, e W. M. Grill, «Modeling the response of small myelinated axons in a compound nerve to kilohertz frequency signals», *J. Neural Eng.*, vol. 14, fasc. 4, p. 046022, ago. 2017, doi: 10.1088/1741-2552/aa6a5f.

[46] J. L. Gaines, K. E. Finn, J. P. Slopsema, L. A. Heyboer, e K. H. Polasek, «A model of motor and sensory axon activation in the median nerve using surface electrical stimulation», *J. Comput. Neurosci.*, vol. 45, fasc. 1, pp. 29–43, ago. 2018, doi: 10.1007/s10827-018-0689-5.

[47] C. C. McIntyre, A. G. Richardson, e W. M. Grill, «Modeling the Excitability of Mammalian Nerve Fibers: Influence of Afterpotentials on the Recovery Cycle», *J. Neurophysiol.*, vol. 87, fasc. 2, pp. 995–1006, feb. 2002, doi: 10.1152/jn.00353.2001.

[48] L. Toni, L. Pierantoni, C. Verardo, S. Romeni, e S. Micera, «Characterization of Machine Learning-Based Surrogate Models of Neural Activation Under Electrical Stimulation», *Bioelectromagnetics*, vol. 46, fasc. 1, p. e22535, 2025, doi: 10.1002/bem.22535.

[49] T. Danka e P. Horvath, «modAL: A modular active learning framework for Python», 12 dicembre 2018, *arXiv*: arXiv:1805.00979. doi: 10.48550/arXiv.1805.00979.

[50] L. Toni, C. Verardo, S. Micera, e S. Romeni, «Influence of Selectivity Metric Choice on Motor Restoration With Neural Electrical Stimulation», in *2025 12th International IEEE/EMBS Conference on Neural Engineering (NER)*, nov. 2025, pp. 1017–1021. doi: 10.1109/NER61569.2025.11588948.

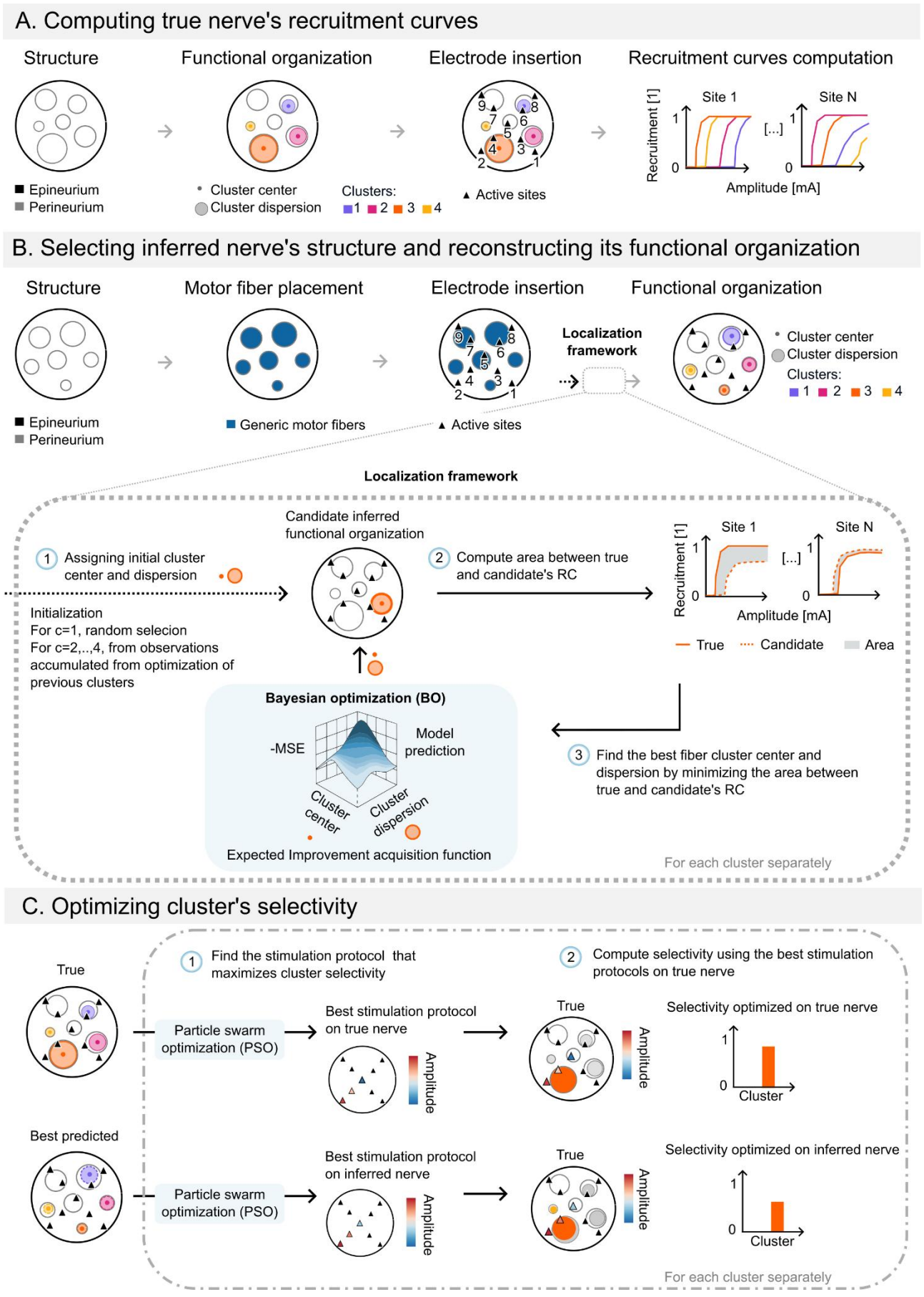


Figure 1: Overview of the proposed framework for reconstructing nerve functional organization and optimizing stimulation selectivity. A. The structural (epineurium and perineurium) and functional

(mapping between fibers and their target clusters) organizations of the true nerve are illustrated. Monopolar RCs are computed for each stimulation site and for each cluster. These curves serve as reference data for reconstructing the inferred functional organization. **B.** Reconstruction of the inferred functional organization. Starting from a nerve with motor fibers uniformly distributed across fascicles, candidate cluster centers and dispersions are sampled within the nerve cross-section. For each cluster, a Bayesian optimization framework iteratively selects candidate parameters to minimize the discrepancy between candidate and reference RCs, quantified as the area between curves. The first cluster is initialized randomly, while subsequent clusters leverage information from previously optimized ones. A Gaussian Process model combined with an Expected Improvement acquisition function guides the search. The resulting cluster parameters define the inferred functional organization. **C.** Optimization of cluster selectivity. For each cluster, particle swarm optimization (PSO) is used to identify the stimulation protocol that maximizes selectivity. Selectivity is computed on both true and inferred nerve organizations, and performance is evaluated on the true nerve.

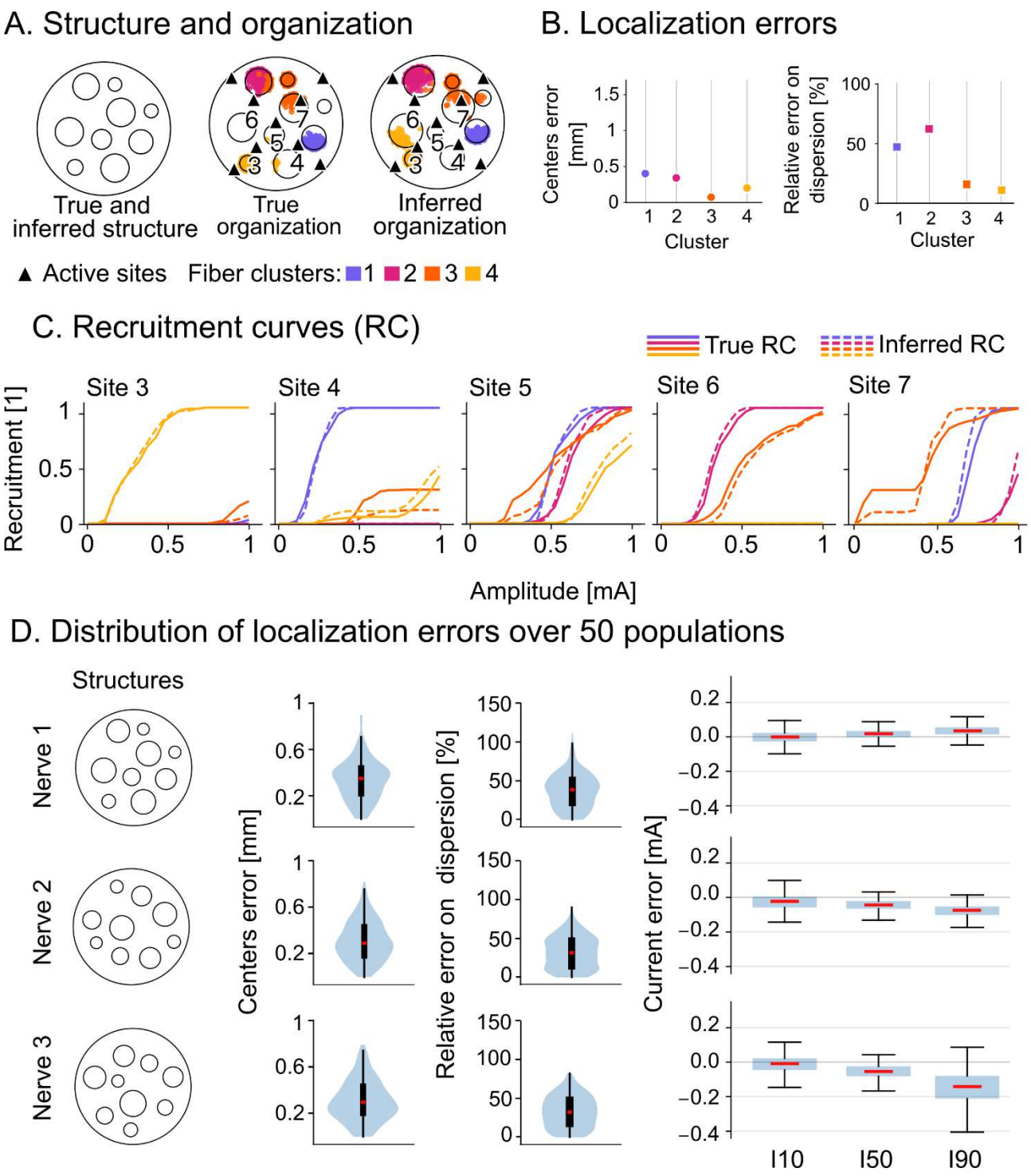


Figure 2. Localization performance and RC reconstruction in simplified nerve models with true structure. A. Example of true and inferred functional organizations within the same structural nerve organization. Fiber clusters (colored) and active stimulation sites (triangles) are shown for both true and inferred cases. **B.** Localization errors for the representative population shown in A, reported as Euclidean distance between true and predicted cluster centers and relative error in cluster dispersion. **C.** Comparison between true (solid lines) and inferred (dashed lines) RCs (RCs) across selected stimulation sites. Each color corresponds to a different fiber cluster. **D.** Distribution of localization errors across 50 populations for three distinct nerve organizations. Violin plots show the distributions of cluster center error (left) and relative dispersion error (middle). Recruitment error (right), computed

as the difference between true and inferred currents corresponding to recruitment levels 0.1, 0.5, and 0.9..

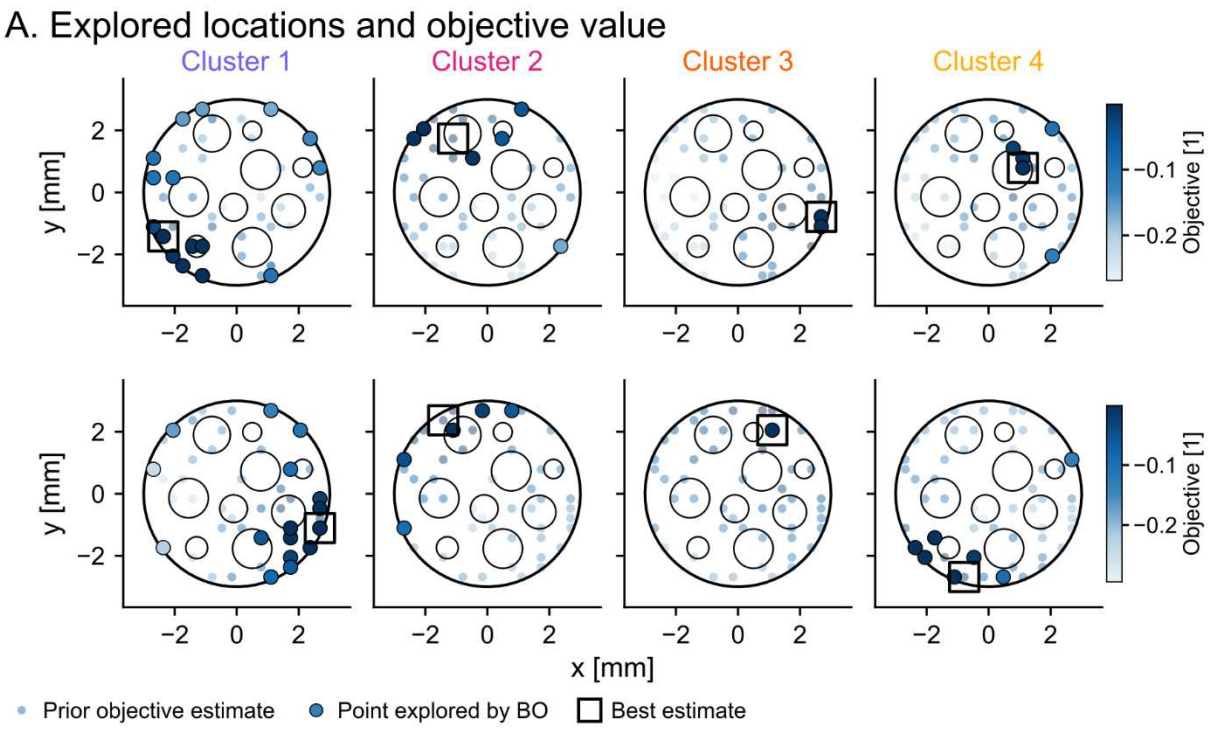

A. Explored locations and objective value
Cluster 1
Cluster 2
Cluster 3
Cluster 4
y [mm]
x [mm]
Objective [1]
Prior objective estimate
Point explored by BO
Best estimate
B. Influence of location and dispersion on the objective
Objective [1]
Δx from best [mm]
Δy from best [mm]
Δσ from best [mm]
C. Iterations and final objective
BO iterations [1]
C1
C2
C3
C4
Tot
Cluster
Final objective [1]
D. Acquisition and stopping criterion
Max EI [1]
Stop threshold
BO iteration [1]
Low EI
Max iters
Populations [1]
Cluster 1
Low EI
Max iters

Figure 3. Behavior of the Bayesian optimization during the localization of fiber clusters. A. Spatial exploration performed by the Bayesian optimization (BO) for each of the four fiber clusters, shown for two representative populations. Each panel reports the nerve cross-section and its fascicles. Light points indicate the candidate configurations constituting the prior objective landscape available at the beginning of the optimization of each cluster: the initial random seed evaluations for cluster 1, and all configurations already evaluated during the optimization of the preceding clusters for clusters 2–4. Outlined points indicate the candidates actively queried during the optimization of the current cluster. All points are colored according to the objective function value. The open square marks the final best estimate of the cluster center. Only the spatial coordinates of each candidate are shown, while the dispersion σ is not represented. **B.** Objective function value as a function of the distance between each evaluated candidate and the best estimate of the corresponding cluster, reported separately for the two spatial coordinates (Δx, Δy) and for the dispersion (Δσ). Gray points pool all candidates evaluated across the four clusters and the 50 populations; the blue line is a quadratic least-squares fit. **C.** Left: mean number of BO iterations required to reach convergence for each cluster and summed over the four clusters; error bars indicate ±1 standard deviation across the 50 populations, with individual populations overlaid as jittered dots. Right: distribution of the final objective value reached for each cluster across the 50 populations, shown as violin plots with median (red line) and individual populations overlaid. **D.** Left: median maximum expected improvement (EI) as a function of the BO iteration for each cluster, with shaded bands indicating the interquartile range across populations; the dashed line marks the EI stopping threshold. Middle: number of populations, out of 50, whose optimization terminated because the maximum EI fell below the threshold (Low EI) or because the maximum number of iterations was reached (Max iters), reported for each cluster. Right: final objective value obtained for cluster 1, grouped according to the stopping criterion that terminated the run.

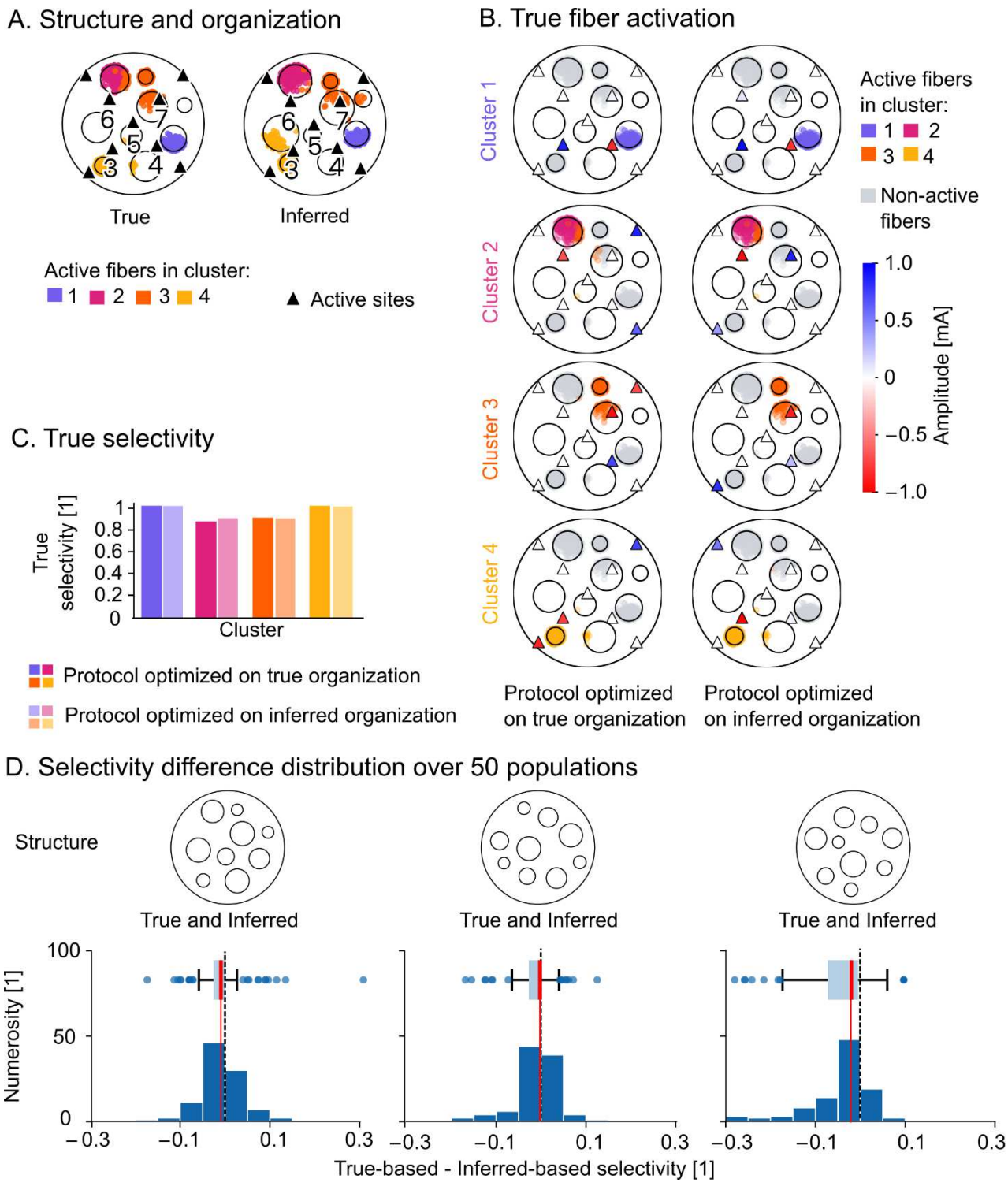


Figure 4. Selectivity optimization using true and inferred functional organizations. A. Representative example of true and inferred functional organizations for a single fiber population. **B.** Fiber activation patterns on the true nerve obtained using stimulation protocols optimized on the true organization (left) and on the inferred organization (right), shown for each cluster. Colored fibers indicate cluster membership, gray fibers are non-active. Triangles denote active stimulation sites, with color intensity representing stimulation amplitude. **C.** Selectivity values computed on the true nerve for each cluster using both true-based and inferred-based stimulation protocols. **D** Distribution of selectivity differences (true-based minus inferred-based) across 50 populations for three distinct nerve organizations.

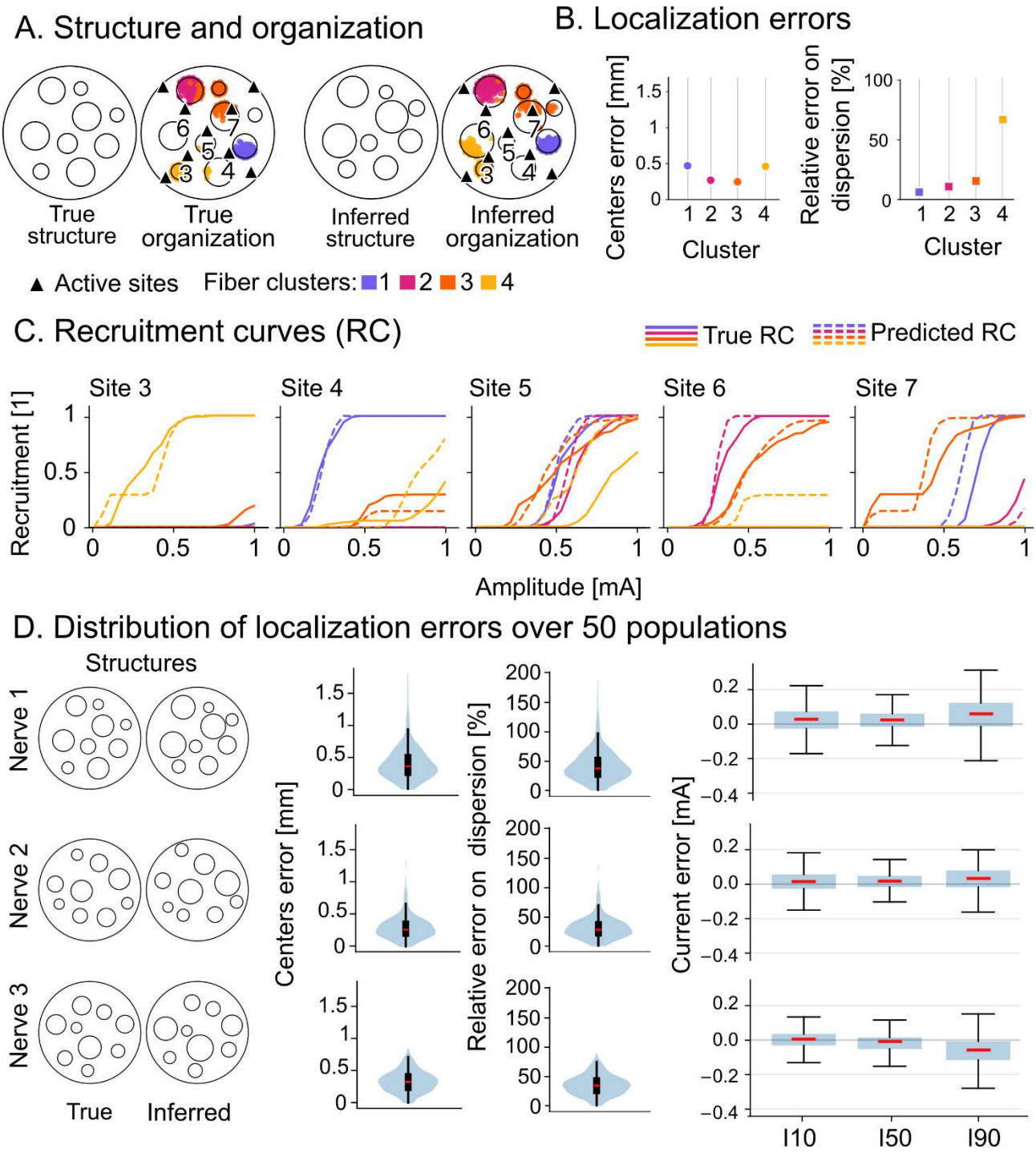


Figure 5. Localization performance and RC reconstruction in simplified nerve models with inexact structure. A. Example of true and inferred structural and functional organizations. Fiber clusters (colored) and active stimulation sites (triangles) are shown. The inferred nerve exhibits perturbed fascicular geometry relative to the true structure. **B.** Localization errors for the representative population shown in (A), reported as Euclidean distance between true and inferred cluster centers and relative error in cluster dispersion. **C.** Comparison between true (solid lines) and inferred (dashed lines) RCs across selected stimulation sites. Each color corresponds to a different fiber cluster. Larger discrepancies are observed compared to the case with matched structure. **D.** Distribution of localization errors across 50 populations for three distinct nerve organizations. Violin plots show the distributions of cluster center error (left) and relative dispersion error (middle). Recruitment error (right), computed as the difference between true and inferred currents corresponding to recruitment levels 0.1, 0.5, and 0.9..

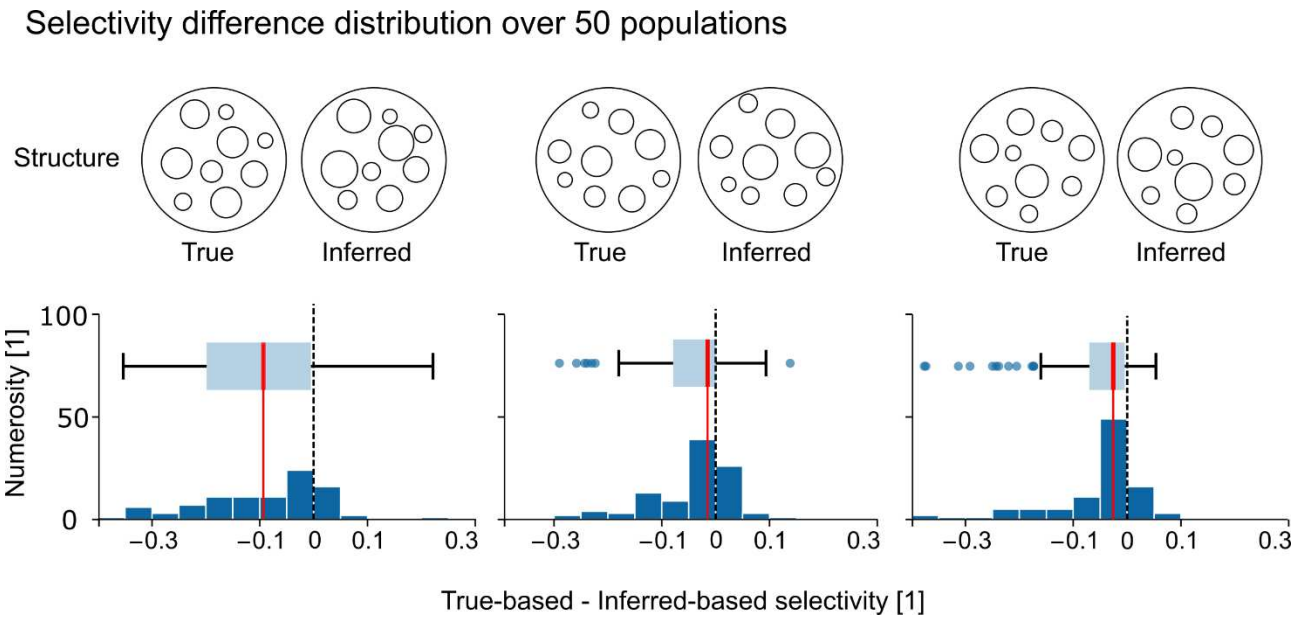


Figure 6. Selectivity optimization in simplified nerve models with inexact structure. Selectivity optimization results in the case in which inferred nerve exhibits perturbed fascicular geometry relative to the true structure. Distribution of selectivity differences (true-based minus inferred-based) across 50 populations for three distinct nerve organizations.

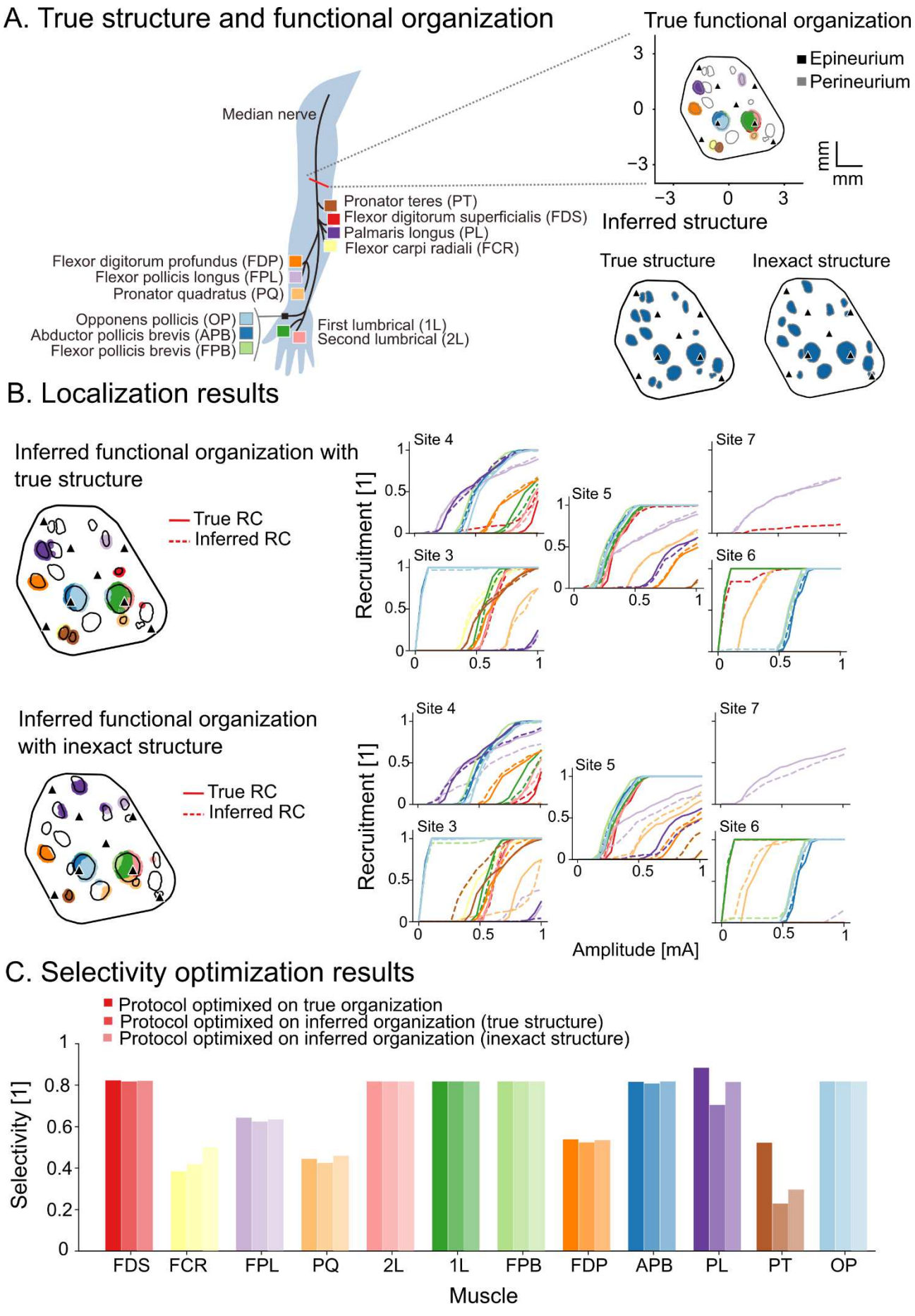
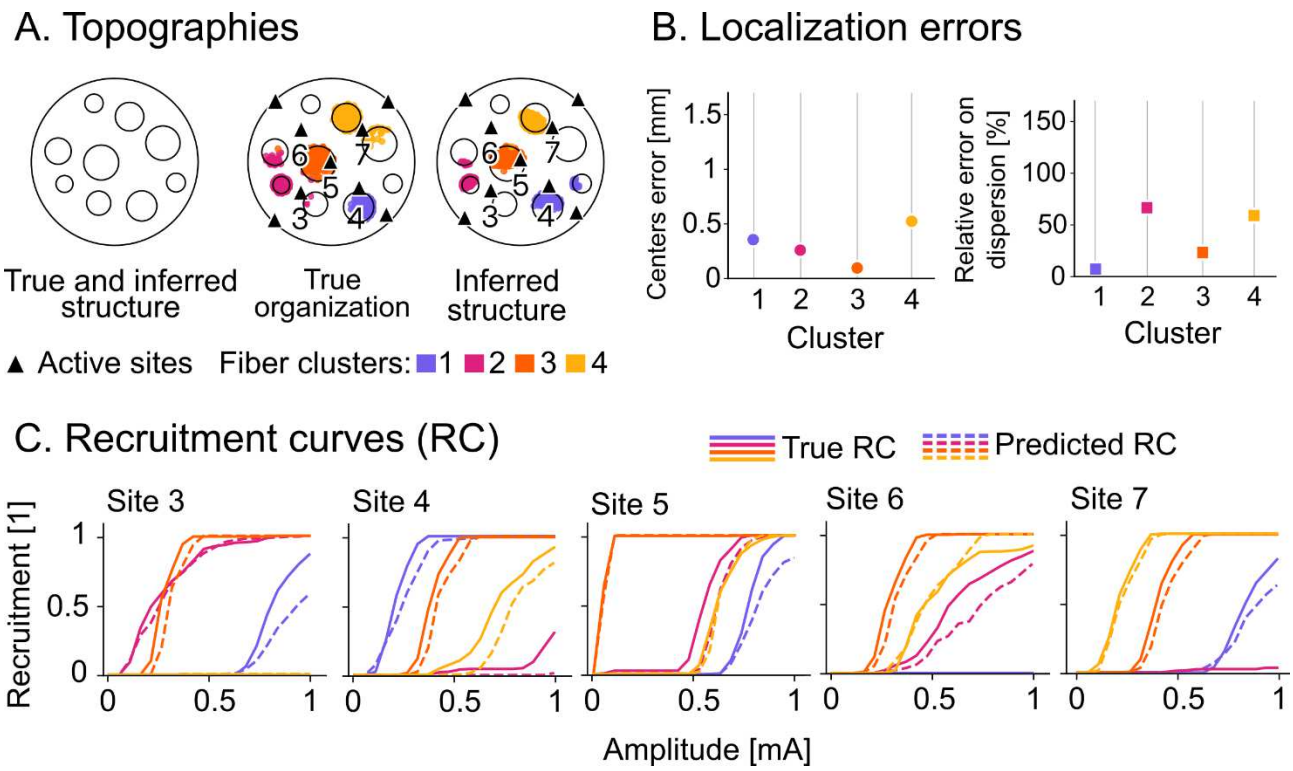

A. True structure and functional organization
True functional organization
Epineurium
Perineurium
3
0
−3
−3
0
3
mm
mm
Median nerve
Pronator teres (PT)
Flexor digitorum superficialis (FDS)
Palmaris longus (PL)
Flexor carpi radiali (FCR)
Flexor digitorum profundus (FDP)
Flexor pollicis longus (FPL)
Pronator quadratus (PQ)
Opponens pollicis (OP)
Abductor pollicis brevis (APB)
Flexor pollicis brevis (FPB)
First lumbrical (1L)
Second lumbrical (2L)
Inferred structure
True structure
Inexact structure
B. Localization results
Inferred functional organization with true structure
True RC
Inferred RC
Site 4
Site 7
Site 5
Site 3
Site 6
Recruitment [1]
Inferred functional organization with inexact structure
True RC
Inferred RC
Site 4
Site 7
Site 5
Site 3
Site 6
Recruitment [1]
Amplitude [mA]
C. Selectivity optimization results
Protocol optimixed on true organization
Protocol optimixed on inferred organization (true structure)
Protocol optimixed on inferred organization (inexact structure)
Selectivity [1]
FDS
FCR
FPL
PQ
2L
1L
FPB
FDP
APB
PL
PT
OP
Muscle

Figure 7. Localization and selectivity optimization results in a nerve section taken from histological segmentation of the human median nerve. A. True median nerve structural and functional organization, and chosen structure for the true structued and inexaxt structure inferred organizations. B. Inferred fiber cluster populations and RC. C. Comparison between true-based, true_structure_based, and inexact_structured_based selectivity.

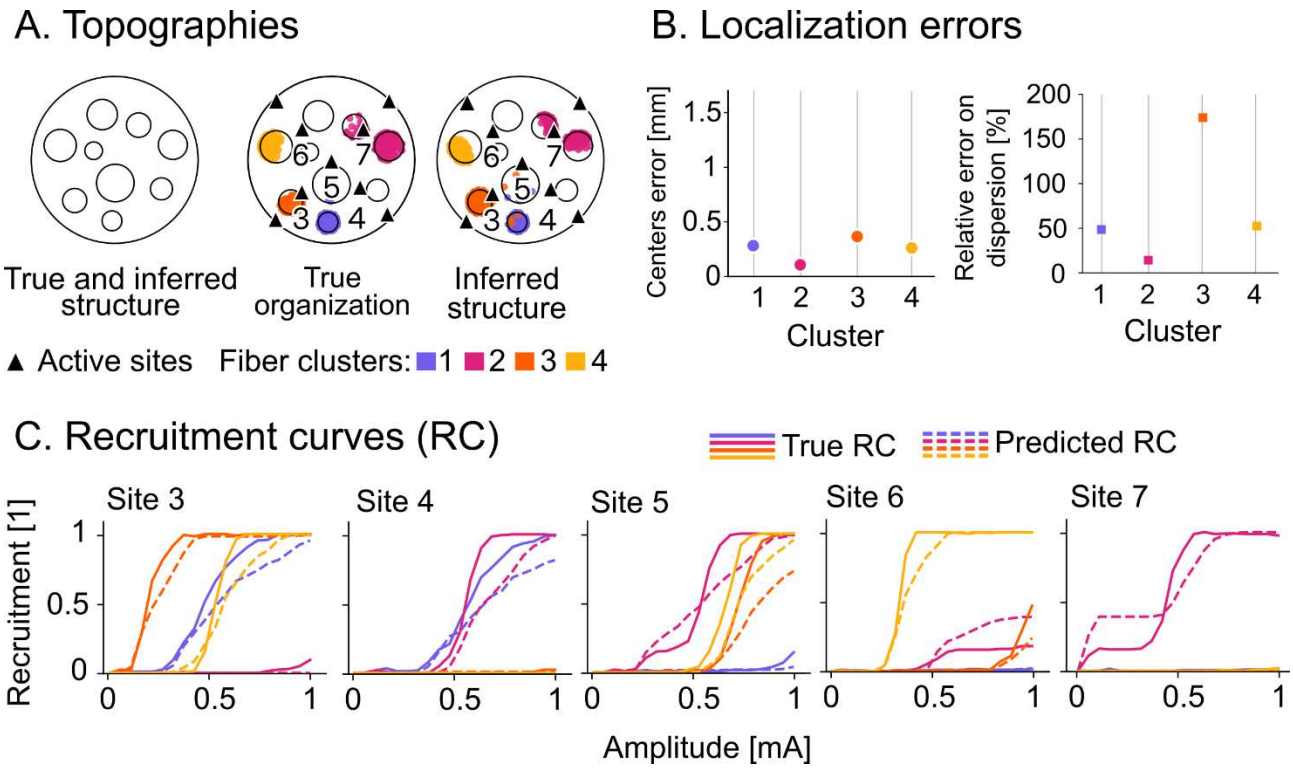
Supplementary Figures

Supplementary Figure 1 – nerve 2



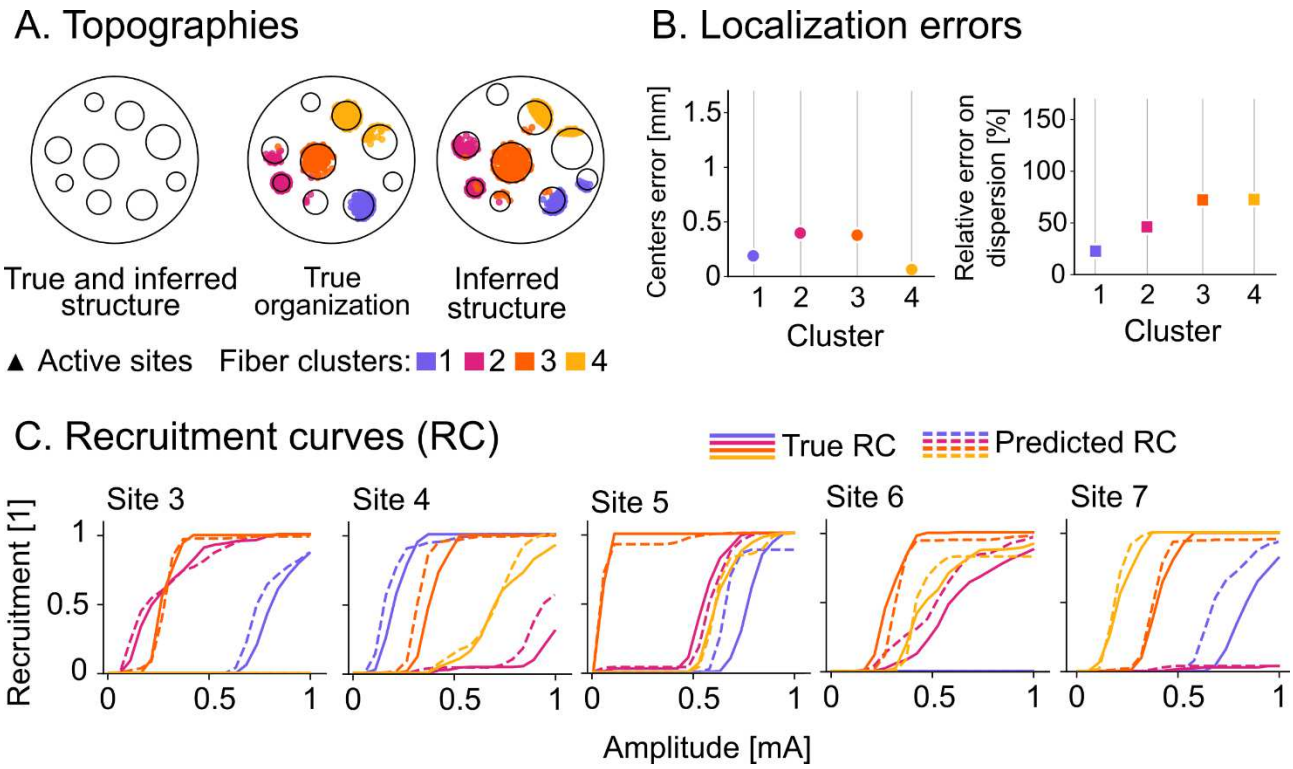
Supplementary Figure 1. True structure localization results. Localization results in the case in which the structure of the inferred organization is the same as for the true nerve (**A**). **B** Functional organizations of the true and inferred nerve for one example nerve and population. Inferred functional organization was inferred though the localization framework. **C** True and inferred RCs. **D** Localization errors, defined as the distance between true and inferred cluster centers (centers distance) and the relative standard error of cluster dispersions.

Supplementary Figure 2 – nerve 3



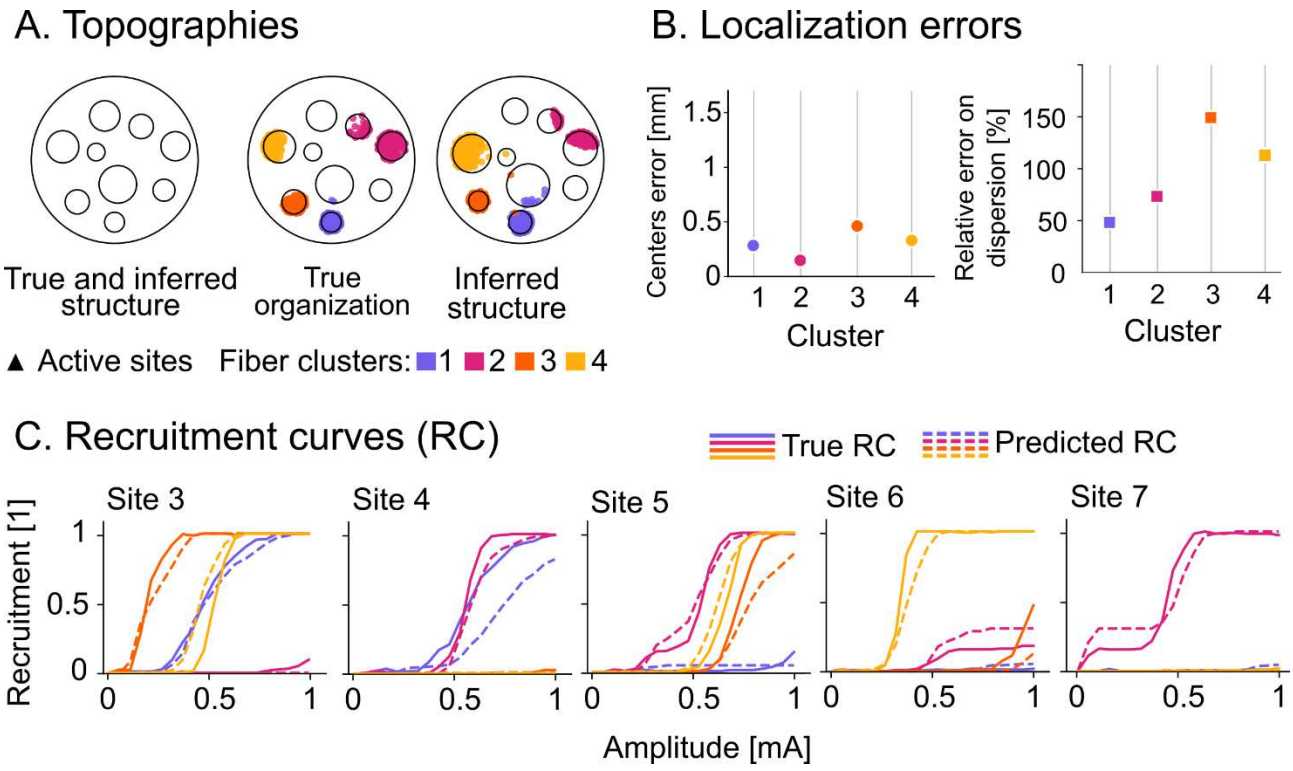
Supplementary Figure 2. True structure localization results. Localization results in the case in which the structure of the inferred organization is the same as for the true nerve (**A**). **B** Functional organizations of the true and inferred nerve for one example nerve and population. Inferred functional organization was reconstructed through the localization framework. **C** True and inferred RCs. **D** Localization errors, defined as the distance between true and inferred cluster centers (centers distance) and the relative standard error of cluster dispersions.

Supplementary Figure 3 – nerve 2 shifted



Supplementary Figure 3. True structure localization results. Localization results in the case in which the structure of the inferred organization is the same as for the true nerve (**A**). **B** Functional organizations of the true and inferred nerve for one example nerve and population. Inferred functional organization was reconstructed through the localization framework. **C** True and inferred RCs. **D** Localization errors, defined as the distance between true and inferred cluster centers (centers distance) and the relative standard error of cluster dispersions.

Supplementary Figure 4 – nerve 3 shifted



Supplementary Figure 4. True structure localization results. Localization results in the case in which the structure of the inferred organization is the same as for the true nerve (**A**). **B** Functional organizations of the true and inferred nerve for one example nerve and population. Inferred functional organization was reconstructed through the localization framework. **C** True and inferred RCs. **D** Localization errors, defined as the distance between true and inferred cluster centers (centers distance) and the relative standard error of cluster dispersions.